



Characterisation of the high-energy neutron field at the ISIS-VESUVIO facility by means of thin-film breakdown counters

A N Smirnov, A V Prokofiev, E E Rodionova, C D Frost,
S Ansell, E Schooneveld, G Gorini, A Pietropaolo

July 2010

©2010 Science and Technology Facilities Council

Enquiries about copyright, reproduction and requests for additional copies of this report should be addressed to:

RAL Library
Science and Technology Facilities Council
Rutherford Appleton Laboratory
Harwell Science and Innovation Campus
Didcot
OX11 0QX

Tel: +44(0)1235 445384
Fax: +44(0)1235 446403
email: library@rl.ac.uk

Science and Technology Facilities Council reports are available online at: <http://epubs.cclrc.ac.uk/>

ISSN 1358-6254

Neither the Council nor the Laboratory accept any responsibility for loss or damage arising from the use of information contained in any of their reports or in any communication about their tests or investigations.

Characterisation of the high-energy neutron field at the ISIS-VESUVIO facility by means of thin-film breakdown counters

Andrey N. Smirnov¹, Alexander V. Prokofiev², Ekaterina E. Rodionova¹, Christopher D. Frost³,
Stuart Ansell³, Eric Schooneveld³, Giuseppe Gorini⁴, Antonino Pietropaolo⁵

1 V.G. Khlopin Radium Institute, St. Petersburg, Russia

2 The Svedberg Laboratory, Uppsala University, Uppsala, Sweden

3 ISIS Facility, Rutherford Appleton Laboratory, Chilton, United Kingdom

4 Dipartimento di Fisica "G. Occhialini," Università degli Studi di Milano-Bicocca, Italy

5 Centro NAST, Università degli Studi di Roma Tor Vergata, Italy

Abstract—High-energy neutron field of the VESUVIO instrument at the ISIS facility has been characterized using the technique of thin film breakdown counters. The work is a part of the project to develop ChipIr, a new dedicated facility for accelerated testing of electronic components and systems for neutron-induced single event effects in the new Target Station 2 at ISIS.

I. INTRODUCTION

Single-event effects (SEE) cause one of the major reliability concerns in semiconductor electronic components and systems [1, 2]. High-energy neutrons, produced by cosmic rays in the Earth's atmosphere, may cause significant or dominating fraction of the SEE rate at aircraft altitudes and even in terrestrial applications, such as automotive, telecom, and others.

The most straightforward way to test a component for neutron SEE is to irradiate it by neutrons with atmospheric-like spectrum and with flux enhanced by many orders of magnitude relative to the atmospheric one. During the last years, dedicated neutron instruments (beam lines) have been constructed for these "accelerated testing" studies. The examples are the ICE House at the LANSCE facility in Los Alamos, USA [3], the flood-beam facility at TRIUMF, Vancouver, Canada [4], and the ANITA facility at TSL, Uppsala, Sweden [5].

A dedicated instrument called ChipIr is being designed for accelerated neutron SEE testing at the ISIS facility in Target Station 2 [6, 7]. An important requirement to the future ChipIr instrument is availability of a real-time measurement technique for the neutron flux in the energy region 1-800 MeV, which is of primary importance for SEE testing. Among high-energy neutron detection techniques considered for implementation at ChipIr, thin-film breakdown counters (TFBC) [8] are promising, due to timing properties, compact design, insensitivity to background particles and gamma-radiation, and long-term stability under heavy radiation conditions. The technique utilizes fission of heavy nuclei by high-energy neutrons.

The present work is a feasibility study for application of the TFBC technique at the ISIS neutron source. Using TFBC with fission samples, we have performed characterization measurements for the high-energy component of the neutron field at the VESUVIO instrument [9, 10] at ISIS Target Station 1, which is also in use for SEE studies [11]. We have measured distributions of fission events in bismuth and uranium samples versus neutron time of flight (TOF). Integration over the measured distributions allowed us to determine the energy-integrated neutron flux. The experimental results are compared with simulations from ref. [11], performed with the MCNPX code [12].

II. METHODOICAL APPROACH

A. The neutron instrument

The neutron production at ISIS relies upon spallation reactions induced by 800-MeV proton bunches accelerated through a synchrotron. The beam makes about 10^4 orbits inside the synchrotron as it is accelerated before being kicked in a single revolution to the extraction beam line, delivering $4 \mu\text{C}$ of protons in two 100-ns-long pulses to a spallation target made of tungsten. The entire acceleration process is repeated with 50 Hz frequency, so that a mean current of $200 \mu\text{A}$ is delivered to the target, with a neutron yield of about 30 neutrons per proton. The VESUVIO instrument, mainly intended for spectroscopy with neutrons in the low-eV range, has a primary flight path of 11.055 m and a water moderator at ambient temperature. The instrument provides a pulsed neutron beam whose spectrum is peaked at about 30 meV and is known to decrease as $1/E^\alpha$, with $\alpha \approx 0.9$, in the epithermal energy region (above 0.5 eV). The undermoderation of neutrons results in the presence of an intense flux of neutrons above 1 MeV. The beam diameter at the sample position is about 4.5 cm. Further information about the VESUVIO instrument may be found in [9-11].

B. Simulated spectral neutron flux

The neutron spectrum at the reference position of the VESUVIO instrument was simulated in ref [11] using the MCNPX code [12]. According to the simulated results, shown in Fig. 1, the spectrum consists predominantly of thermal and epithermal neutrons. More than 80% of neutrons possess energies below 100 keV. A high-energy component (1-800 MeV) contains $\approx 7\%$ of all neutrons.

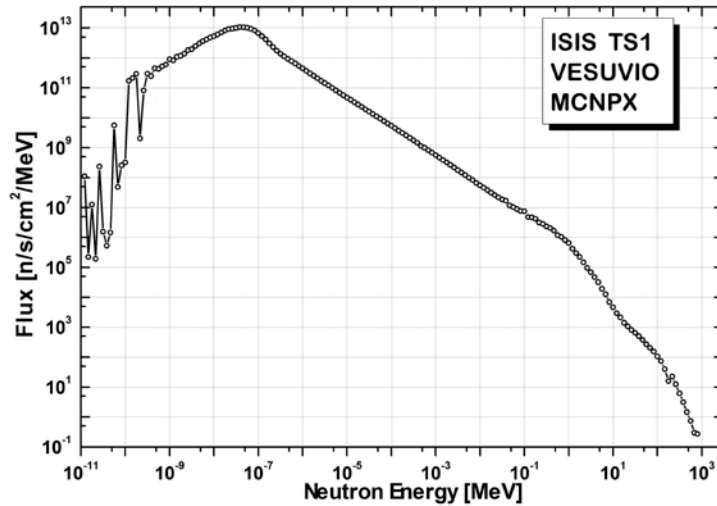


Figure 1. Spectral neutron flux at the VESUVIO instrument at the ISIS neutron source, calculated with the MCNPX code [11]. The data relate to the reference position (1105.5 cm from the frontal surface of the moderator) and to the primary proton beam current of $180 \mu\text{A}$.

C. Fission cross sections

The principle of the high-energy neutron flux measurement is based on detection of fragments that originate from neutron-induced fission of heavy nuclei. In this work, we used neutron-induced fission reactions for ^{nat}U and ^{209}Bi . Due to high fission thresholds, ≈ 1 MeV for ^{238}U (the main constituent of ^{nat}U) and ≈ 20 MeV for ^{209}Bi , these reactions are suitable for neutron flux measurements at the high-energy part of the ISIS neutron spectrum.

Experimental cross-section data for the considered (n,f) reactions are available at energies up to ≈ 200 MeV [13-17]. A lack of experimental (n,f) data above 200 MeV can be remedied by a joint analysis of cross section data for neutron- and proton-induced fission reactions, which show broad physical similarity at high energies. As concluded in ref [18], the cross-section ratio σ_{pf}/σ_{nf} exhibits very weak or no dependence on the incident energy above ~ 150 MeV for nuclei from Pb to Np. The ratio σ_{pf}/σ_{nf} at higher energies was found to depend systematically on the nucleon composition of the fissioning nuclei [18].

For proton-induced fission, an abundant cross-section database exists [19]. The analysis of the database in ref [19] resulted in systematics of (p,f) cross sections for target nuclei from ^{165}Ho to ^{239}Pu , at the range of incident energies from 20 MeV to 30 GeV, and a universal parameterization was suggested:

$$\sigma_{pf}(E_p) = P_1 \cdot \{1 - \exp[-P_3 \cdot (E_p - P_2)]\} \cdot (1 - P_4 \cdot \ln E_p), \quad (1)$$

where $\sigma_{pf}(E_p)$ is the fission cross section, E_p is the incident proton energy, and $P_1 \dots P_4$ are fitting parameters that depend regularly on the "fissility parameter" Z^2/A , where Z and A are the charge and the mass of the corresponding composite system (incident nucleon + target nucleus).

In the present work, we have used existing (n,f) cross section data up to ≈ 200 MeV [13, 14] and extended them up to 800 MeV by following the cross-section shape predicted by the systematics of ref [19]. The details are given below separately for different fission reactions used.

1. The $^{209}\text{Bi}(n,f)$ cross section

A universal cross-section parameterization was suggested in ref [13] for fission of nuclei from Ta to Bi in the neutron energy range from 30 to 180 MeV. In order to extend the $^{209}\text{Bi}(n,f)$ cross-section dependence up to 800 MeV, we have assumed that the cross-section shape in the 180-800 MeV range can be described by Eq. (1), i.e. by the same functional form that was found in ref [19] for proton-induced fission. The parameters $P_1 \dots P_4$ were calculated using the systematics [19] for the composite system $^{209}\text{Bi} + n$, and the resulted cross section curve was re-normalized with a factor 0.968 for a smooth connection to the parameterization of ref [13]¹. The final values of the parameters $P_1 \dots P_4$ are given in Table 1, and the adopted $^{209}\text{Bi}(n,f)$ cross section is plotted in Fig. 2.

Neutrons with energies below 30 MeV give a contribution of less than 0.05% to the overall response of ^{209}Bi monitors to the VESUVIO neutron field, as follows from an estimate based on the simulated spectral neutron flux [11] and on the parameterization of ref [13], extrapolated to lower energies, where it is known to overestimate the cross section. Thus, fission of ^{209}Bi by neutrons below 30 MeV could be neglected.

¹ Thus, only a minor re-normalization of the cross-section dependence was required. This strengthens our confidence in the cross-section parameterizations used in the present work.

2. The $^{238}\text{U}(n,f)$, $^{235}\text{U}(n,f)$, and $^{\text{nat}}\text{U}(n,f)$ cross sections

The $^{238}\text{U}(n,f)$ and $^{235}\text{U}(n,f)$ cross sections were taken from the ENDF library [20] and from the recent IAEA standard [14], at the neutron energy range 0-20 MeV and 20-200 MeV, respectively. At energies 200-800 MeV, application of Eq. (1) with parameters from ref. [19] allowed us to reduce it to a simpler form:

$$\sigma_{nf}(E_n) = P_1 \cdot (1 - P_4 \cdot \ln E_n), \quad (2)$$

where σ_{nf} is the fission cross section and E_n is the incident neutron energy (MeV). Finally, the parameter P_1 was chosen for a smooth connection to the data of ref [14] at the energy of 200 MeV. The adopted values of the parameters P_1 and P_4 are given in Table 1.

The $^{\text{nat}}\text{U}(n,f)$ cross section was calculated by weighted summation of the cross sections for ^{238}U and ^{235}U with weights corresponding to the abundance ratios of these isotopes in $^{\text{nat}}\text{U}$. The adopted $^{\text{nat}}\text{U}(n,f)$ cross section is plotted in Fig. 2.

Table 1. The summary of the adopted fission cross section data.

Neutron energy range (MeV)	Functional form or data source	Parameters			
		P_1 (mb)	P_2 (MeV)	P_3 (^a)	P_4 (no-dim)
$^{209}\text{Bi}(n,f)$					
0-30	$\sigma_{nf}(E_n) = 0$	-	-	-	-
30-180	$\sigma_{nf}(E_n) = P_1 \exp[-(P_2/E_n)^{P_3}]$ [13]	109.2	131.5	1.32	-
180-800	$\sigma_{nf}(E_n) = P_1 \{1 - \exp[-P_3(E_n - P_2)]\} (1 - P_4 \ln E_n)$	113.0	50.40	$5.982 \cdot 10^{-3}$	$1.473 \cdot 10^{-2}$
$^{238}\text{U}(n,f)$					
0-20	Tabulated data from ref [20]	-	-	-	-
20-200	Tabulated data from ref [14]	-	-	-	-
200-800	$\sigma_{nf}(E_n) = P_1 (1 - P_4 \ln E_n)$	2036.7	-	-	0.067
$^{235}\text{U}(n,f)$					
0-20	Tabulated data from ref [20]	-	-	-	-
20-200	Tabulated data from ref [14]	-	-	-	-
200-800	$\sigma_{nf}(E_n) = P_1 (1 - P_4 \ln E_n)$	2244.6	-	-	0.067

^a In the formulas for the $^{209}\text{Bi}(n,f)$ cross section, the parameter P_3 has different dimension units in the energy regions 30-180 MeV and 180-800 MeV, respectively non-dimensional units and MeV^{-1} .

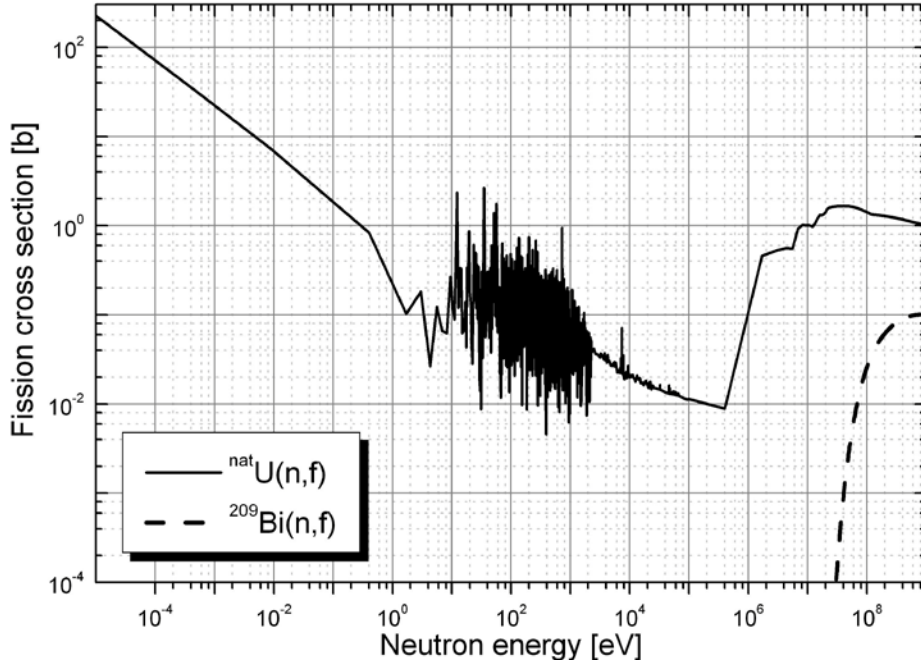


Figure 2. The neutron-induced fission cross sections of ^{209}Bi and $^{\text{nat}}\text{U}$ adopted in the present work.

D. Basics of the TFBC technique

We used TFBC [8] for detection of fragments originating from neutron-induced fission. The operation principle of the TFBC is based on the phenomenon of electric breakdown in a MOS structure caused by a heavy ion, e.g. a fission fragment, passing through a thin silicone dioxide layer (see Fig. 3). The breakdowns are non-shorting, since they lead to vaporization of a small part of the electrode area and leave no conducting path between the electrodes.

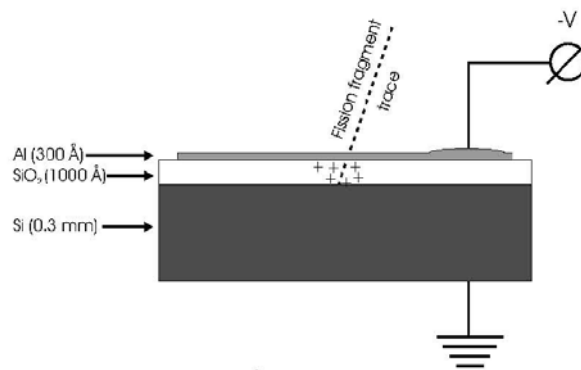


Figure 3. Layout of TFBC and principle of its operation. An incident fission fragment produces an electrical breakdown in the SiO_2 layer.

TFBCs offer real-time operation, time resolution in sub-nanosecond scale, and compact design. They are capable of operation in harsh radiation environments, due to their insensitivity to charged particles with LET below $\approx 15 \text{ MeV}\cdot\text{mg}/\text{cm}^2$ in silicon dioxide, i.e. to protons, deuterons, α -particles and other light ions up to Ne. Neither are TFBCs sensitive to neutrons or γ -rays. These properties

constitute advantages of TFBCs over semiconductor detectors and gas-filled ionization fission chambers, which are sensitive to light ionizing particles and γ -rays produced by the primary beam in detector and sample materials.

Since the VESUVIO neutron beam has relatively low flux at energies above ~ 1 MeV, it is necessary to use TFBCs in sandwich geometry, i.e. the detector has to be situated as close as possible to the fission sample. The sensitive area of the detector is fully covered by the area of the fission sample. The sample-detector sandwich and its mechanical housing constitute a TFBC-based monitor, which is placed in the neutron beam. The amount of material in a monitor chamber along the beam direction is dominated by the thickness of the TFBC (0.3 mm Si). Consequently, the probability of interaction of an incident neutron with the chamber is small, and it is possible to stack several chambers after each other in the neutron beam without significant influence on the beam characteristics.

E. Detection efficiency of TFBC and sensitivity of neutron monitors

In the sandwich geometry, a TFBC does not detect *all* fission events that happen in the sample. Fragments with low LET, as well as fragments arriving at “grazing” angles, are not detected. The fraction of fissions in the monitor sample that result in a breakdown in the TFBC, further referred as the *detection efficiency* of the TFBC, depends on the TFBC bias voltage, on the properties of the TFBC sensitive surface, as well as on the distribution of incident fission fragments over LET and over angle to the surface. That distribution, in turn, depends on the neutron energy, on the direction of the incident neutron flux, as well as on the chemical composition and thickness of the fission sample. In neutron monitoring practice, it is feasible to achieve the detection efficiency of ≈ 30 -40%.

Accurate determination of the detection efficiency is the most challenging element in the application of TFBC for monitoring of high-energy neutron beams. A lack of calibrated monoenergetic beams of high-energy neutrons makes it impossible to determine directly the detection efficiency, or the sensitivity of a TFBC-based monitor. On the other hand, one can determine the detection efficiency ε_{sf} for spontaneous fission fragments, using e.g. a sample that contains ^{252}Cf nuclei:

$$\varepsilon_{sf} = \frac{n_{sf}}{S_{TFBC} a_{sf}}, \quad (3)$$

where n_{sf} is the count rate of spontaneous fission fragments in such “calibration” measurement, S_{TFBC} is the sensitive area of the TFBC, and a_{sf} is the areal density of spontaneous fission activity of the ^{252}Cf calibration sample, which has to be determined in an independent measurement with conventional techniques.

For a TFBC-based monitor, located in a uniform neutron field with the spectral neutron flux density $\varphi(E_n)$, the count rate of fragments that originate from neutron-induced fission is:

$$n_f = \int_{E_{nmin}}^{E_{nmax}} \varphi(E_n) \cdot s(E_n, A, p_A) \cdot dE_n, \quad (4)$$

where E_{nmin} and E_{nmax} are the minimum and the maximum energy in the neutron spectrum, respectively, and $s(E_n, A, p_A)$ is the spectral sensitivity of the monitor:

$$s(E_n, A, p_A) = p_A \cdot \sigma_{nf}(E_n, A) \cdot S_{TFBC} \cdot \varepsilon_{nf}(E_n, A, p_A), \quad (5)$$

where p_A is the number of fissionable nuclei with the atomic mass A per unit of monitor sample area, $\sigma_{nf}(E_n, A)$ is the fission cross section, and $\varepsilon_{nf}(E_n, A, p_A)$ is the detection efficiency of the TFBC for the given monitor sample. In order to account for the difference between the detection efficiencies for the monitor sample and the calibration one, the correction factor k_ε is introduced:

$$k_\varepsilon(E_n, A, p_A) = \frac{\varepsilon_{nf}(E_n, A, p_A)}{\varepsilon_{sf}}. \quad (6)$$

By combining Eqs. (3), (5), and (6), we obtain:

$$s(E_n, A, p_A) = p_A \sigma_{nf}(E_n, A) \tilde{\varepsilon}_{sf} k_\varepsilon(E_n, A, p_A), \quad (7)$$

where

$$\tilde{\varepsilon}_{sf} = \frac{n_{sf}}{a_{sf}} \quad (8)$$

is the reduced detection efficiency, which is determined in the calibration with a ^{252}Cf sample.

In Eq. (7), the term S_{TFBC} is cancelled out, and thus an independent determination of the sensitive area of the TFBC is not necessary. The term p_A is determined in characterisation measurements for the monitor samples (see Sect. III.A). The term $\sigma_{nf}(E_n, A)$ is discussed in Sect. II.C. Finally, the correction term $k_\varepsilon(E_n, A, p_A)$ is determined using the COUCH code [21], which allows one to simulate the process of particle detection by a TFBC. The COUCH code was used earlier in the range of incident nucleon energies up to ≈ 200 MeV [13]. In order to perform the similar calculations for neutron energies up to 800 MeV, we have utilized the following input data:

- the linear momentum transfer and the angular anisotropy in fission reactions, parameterized by Prokofiev [22],
- fission fragment mass distributions in the reaction $^{238}\text{U}(n,f)$, measured by Zöller [23].

The fragment mass distributions [23] show only minor variations versus incident neutron energy in the range from 180 MeV to the highest energy explored in Ref. [23], 450 MeV. We have assumed that the mass distribution does not depend on the neutron energy at the range 180-800 MeV. Data of this type for neutron-induced fission of subactinide nuclei remain unmeasured. Therefore, for $^{209}\text{Bi}(n,f)$ reaction we used symmetric Gaussian-shaped mass distributions that are typical for similar fissioning systems formed in reactions of charged particles with subactinide nuclei [24]. Uncertainties originating from these assumptions are expected to have negligible influence on the calculated corrections to the detection efficiencies.

F. Verification of the spectral neutron flux using TOF techniques

The temporal structure of the primary proton beam at the ISIS facility is shown in Fig. 4a [25]. The beam is extracted in two pulses, each of ≈ 100 ns duration, with ≈ 200 ns interval. Such temporal structure is not favourable for direct TOF measurements at high neutron energies. Still, neutron spectrum information can be derived indirectly, using either an unfolding procedure or a comparison of the experimental temporal distributions with simulated ones. Only the second option has been explored in this report.

Simulations of temporal distributions of fission events versus neutron TOF have been performed using the “Time-of-Flight vs. Energy _ Monte Carlo” (TFE_MC) code [26] with the assumption about a point-wise virtual neutron source located at the surface of the moderator. The input data for the simulations included the temporal structure data [25], the adopted fission cross sections (see Sect. II.C), the neutron spectrum simulated with the MCNPX code [11], the flight distances, and the time resolution of the monitors. The simulated temporal distributions of fission events in monitors with ^{209}Bi and $^{\text{nat}}\text{U}$ samples are shown in Fig. 4b and 4c, respectively.

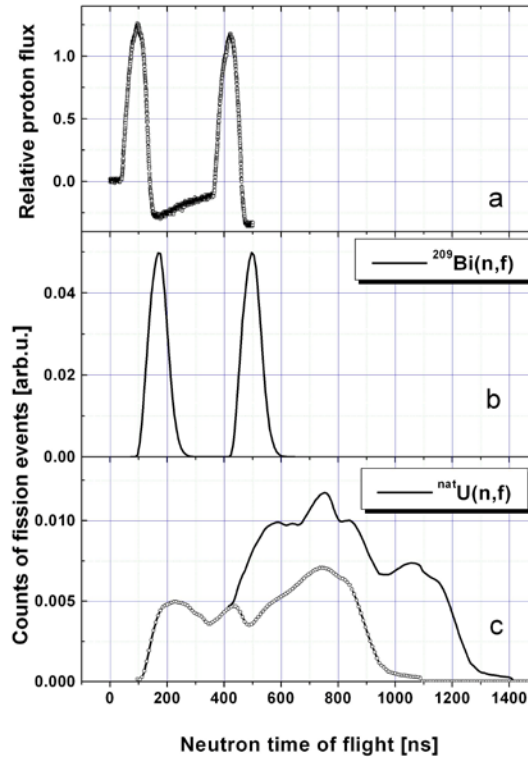


Figure 4. Temporal structure of the ISIS proton beam (a) and the simulated TOF distributions of fission events in monitors with ^{209}Bi (b) and $^{\text{nat}}\text{U}$ (c) at ~ 13 m distance from the neutron source. The dashed curve at the panel (c) corresponds to the TOF distribution of the ^{238}U fission events induced by neutrons originating from the first proton pulse in the double-pulse structure.

III. EXPERIMENTAL ARRANGEMENT

A. Detectors and samples

A few TFBC-based neutron monitors were installed at the neutron path in the VESUVIO blockhouse. During the experiment, different combinations of monitors were used, which included TFBCs of n -type and p -type [27] with samples of $^{\text{nat}}\text{U}$ and ^{209}Bi , located at distances of 1160, 1225, and 1296 cm from the neutron source². For a part of the experiment, we used monitors that consisted of a few detector-target sandwiches, arranged in a stack.

² Here and further in the text, we use the term “distance from the neutron source” in the meaning “distance from the surface of the moderator”, unless otherwise specified.

Characteristics of the fission samples are documented in Table 2. The samples were characterized using conventional techniques (α -spectrometry for the samples of ^{235}U , direct mass determination and/or Rutherford backscattering spectrometry for the samples of ^{209}Bi).

Table 2. The fission sample data.

Fission nuclide	Chemical form	Number of samples	Areal density (mg/cm^2)	Error (%)	Diameter (cm)
^{209}Bi	Bi	4	2.05; 2.06; 2.06; 2.21	3.0	1.70
^{235}U	U_3O_8	3	2.00	3.0	1.70

The diameter of the sensitive surface of each fission sample and each TFBC amounted to ≈ 1.7 cm. Since the diameter of the central homogeneous area of the neutron beam spot amounted to ≈ 2 cm, all the monitors were uniformly irradiated. Figure 5 illustrates the disposition of the monitors and supporting pulse shapers at the neutron beam path.

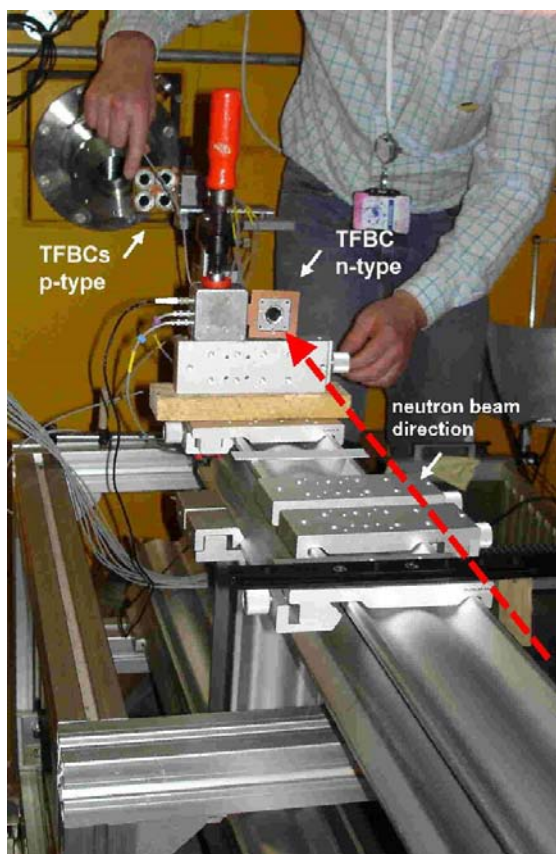


Figure 5. Disposition of the TFBC-based monitors at the VESUVIO beam path. Samples are not installed yet.

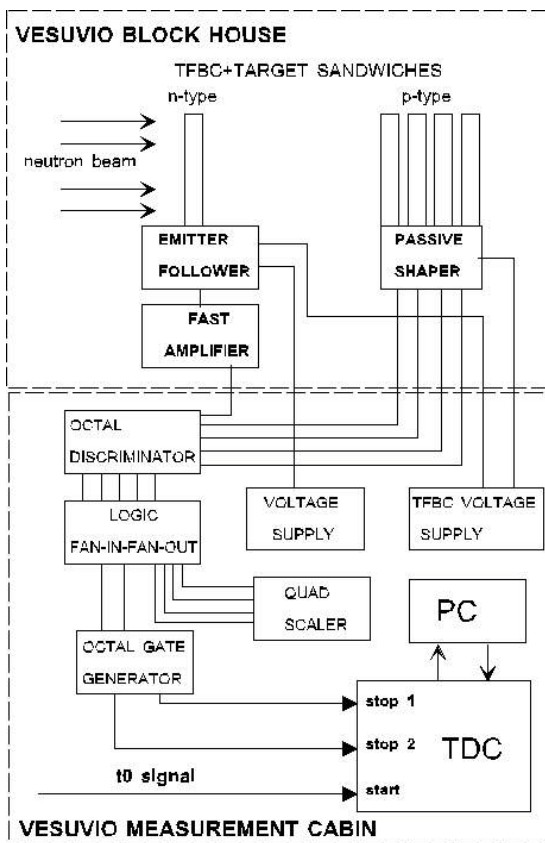


Figure 6. A block diagram of the experimental setup, the electronics, and the data acquisition system.

B. Electronics and data acquisition

In Fig. 6, a block diagram of the experimental setup is presented, including the electronics and the data acquisition system. The following electronic modules were used:

- Amplifier Phillips Scientific 776
- Discriminator LeCroy 4608C
- Logic Fan-In-Fan-Out LeCroy 429
- Gate generator GG8020
- Scaler Ortec 976
- TDC FastComTech, embedded in a PC with MCDWIN software [28].

Pulses from the n -type TFBC were amplified by a factor of 100 prior to sending them to the VESUVIO measurement cabin through a 30-m long cable. Pulses from the p -type TFBC did not require amplification. The scaler with manual control was used for counting of discriminated TFBC pulses without timing selection.

The t_0 pulse, phase-locked to the extraction of the proton beam from the synchrotron, was employed as the start of the TDC. The two available TDC channels were independently stopped by discriminated TFBC pulses. Before arriving at the TDC, the TFBC pulses were delayed by $\approx 2 \mu\text{s}$, in order to compensate for a delay in the t_0 pulse circuit, which was not accurately known. The software for the TDC allowed us to obtain temporal distributions of fission events registered by two independent monitors.

The similar experimental technique was earlier implemented at the TSL neutron facility in Uppsala [5].

IV. EXPERIMENTAL RESULTS

A. Distributions of fission events versus neutron TOF

Fig. 7 presents a relative temporal distribution of events in a monitor with a ^{nat}U sample located at the VESUVIO blockhouse at a distance of 1296 cm, obtained experimentally (at the lower panel) and calculated using the TFE_MC code (at the upper panel). The input parameters of the simulation included the spectral neutron flux from ref. [11] and the ^{nat}U fission cross section in the neutron energy range from 10^{-5} eV to 800 MeV (see Sect. II.C). Here and in further simulations, the integral area of the calculated distribution is equal to the experimental one. Notice the double logarithmic scale in the graph, the TDC channel width of $4 \mu\text{s}$ and the delay $\approx 8 \mu\text{s}$ of the TFBC pulses relatively to the t_0 start signal. Events in channel #2, that constitute $\sim 7\%$ of the spectrum-integrated number of counts, can be attributed to fission of uranium by neutrons in the energy range from ~ 100 keV to 800 MeV. All other events are believed to originate from fission of ^{235}U , which is present in ^{nat}U , by neutrons with energies below ~ 100 keV. Qualitative agreement is observed between the experimental spectrum and the simulated one.

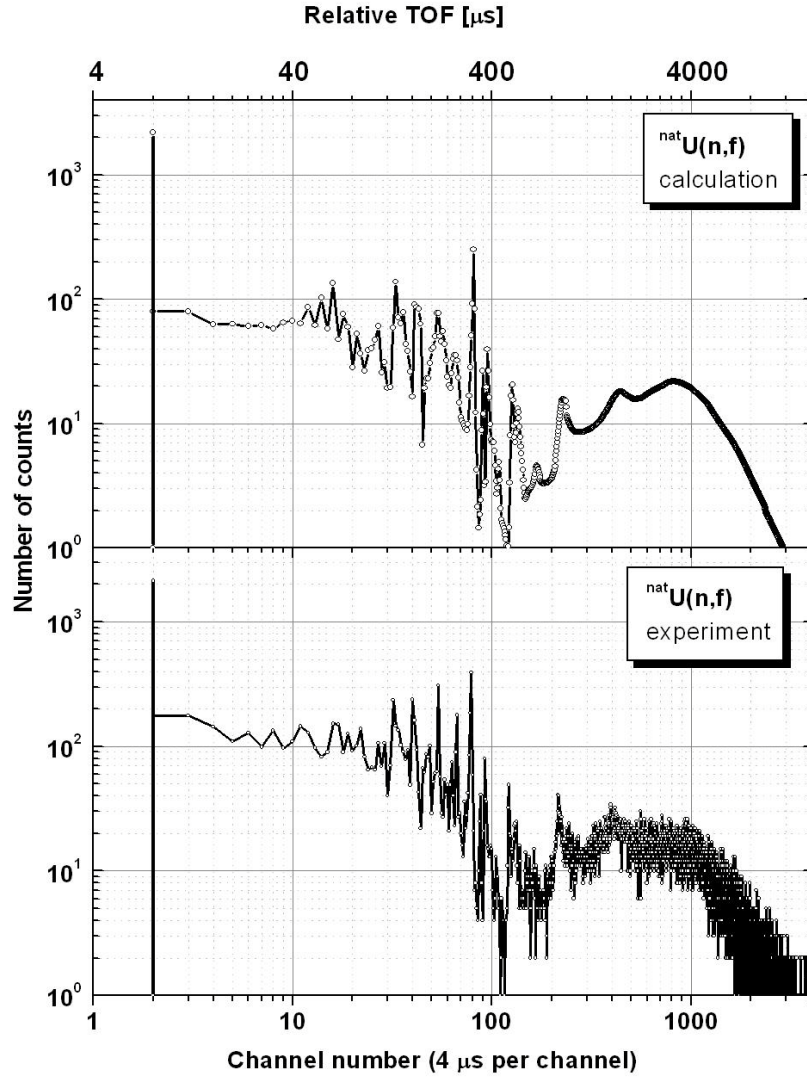


Figure 7. An experimental relative TOF distribution of events in a monitor with a ^{nat}U sample located at the VESUVIO blockhouse, obtained with the TDC with 4- μs channel width (lower panel) and its simulation using the TFE_MC code (upper panel).

Further measurements were carried out with shielding of the monitors by means of a B_4C sheet placed upstreams in order to reduce the overload of the TFBC with the ^{nat}U samples by fission events of ^{235}U by neutrons with energies below ≈ 100 keV.

Fig. 8 presents experimental distributions of fission events in the ^{209}Bi and ^{nat}U samples, obtained at the different positions at the VESUVIO blockhouse with the TDC channel width of 8 ns, together with simulations performed with the TFE_MC code. As it was expected, the $^{209}\text{Bi}(n,f)$ fission events are concentrated in two peaks corresponding to the temporal structure of primary proton beam (see Fig. 4a). The $^{nat}\text{U}(n,f)$ fission events in the spectrum region between channels #7 and #170 (panels a, b, and c) are attributed predominantly to fission of ^{238}U by neutrons in the energy range from ≈ 1 MeV to 800 MeV. The given spectrum region corresponds to the time window of ≈ 1.2 μs duration after the arrival of the first of the two proton pulses at the production target. Events outside of that window are believed to originate from fission of ^{235}U by neutrons with energies below ≈ 1 MeV.

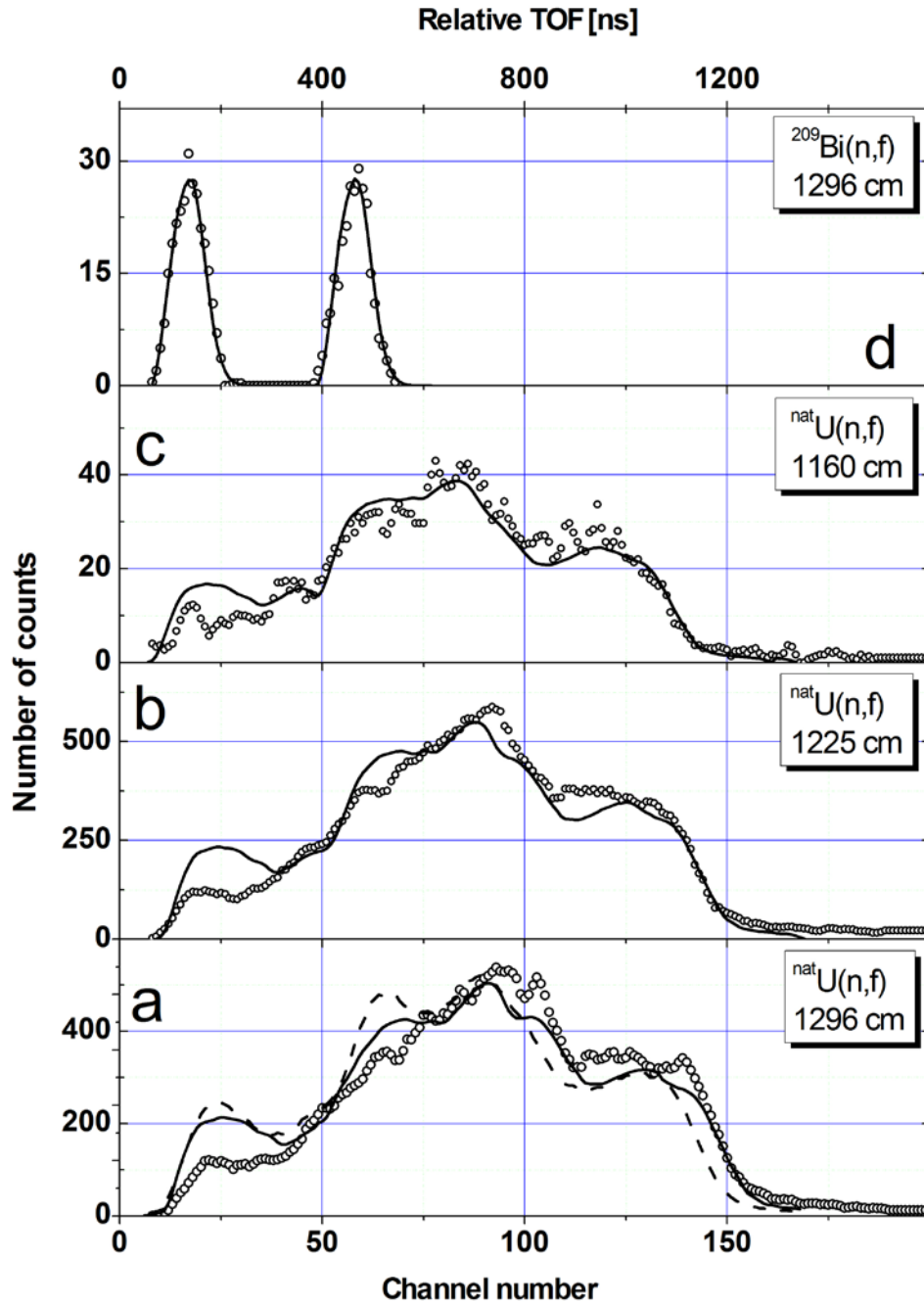


Figure 8. TOF distributions of fission events in the ^{209}Bi and $^{\text{nat}}\text{U}$ samples, obtained at different distances from the neutron source: 1296 cm (a, d), 1225 cm (b) and 1160 cm (c). The TDC channel width is 8 ns. Solid curves represent simulations with the TFE_MC code using increased distances: 1396 cm (a,d) 1325 cm (b) and 1260 cm (c), dashed line (a) represent simulation using the real distance 1296 cm.

Comparing Figs. 8 a, b, and c, one can notice that the experimental temporal distributions of the $^{\text{nat}}\text{U}$ fission events become wider with the increase of the neutron flight path. On the other hand, in order to reproduce the total width of the experimental distributions, we had to increase the flight distances at the simulations by 100 cm (see Fig. 8a-d). In Fig. 8a, two calculated distributions are shown. The dashed line corresponds to the flight path of 1296 cm, i.e. to the assumption that the effective neutron source is located at the surface of the moderator. The solid line, which provides

better agreement with the experiment, corresponds to the flight path of 1396 cm. Thus, we have to assume that the effective source is located “upstream” of the moderator surface.

Qualitative agreement is observed between the simulation curves and the experimental distributions in general. On the other hand, a significant disagreement is seen in the beginning of the distributions for the ^{nat}U monitors, in first 30-40 channels corresponding to incident neutron energy range from ≈ 10 to 800 MeV for neutrons originating from the first pulse of the primary proton beam in the double-pulse structure (see more detailed analysis in Sect. V.B).

B. Count rates of fission monitors

Experimental count rates of fission events were extracted from the measured TOF spectra by summation of the counts in channels corresponding to neutrons in the energy range 1 – 800 MeV, taking into account the temporal structure of the proton beam. The experimental and calculated count rates for different monitors are presented in Table 3. The experimental results are averaged over several measurement series. The quoted uncertainties of the experimental results represent statistical errors only. The calculated results have been obtained with Eq. (4), using the spectral neutron flux above 1 MeV [11], the adopted fission cross sections from Sect. II.C, and the sensitivity of the monitors, see Sect. II.E. The quoted uncertainties of the calculated results include:

- uncertainties in the adopted fission cross sections (2-10%),
- statistical errors in calibration of the TFBCs (3-8%),
- uncertainties in the correction to detection efficiency (5%),
- uncertainties in the areal density of the samples (3%).

Table 3. Experimental and calculated count rates of fission monitors

Neutron energy range MeV	Sample	Number of samples	Distance from the source (cm)	Experimental count rate (1/s)	Calculated count rate (1/s)**
10^{-11} – 800*	^{nat}U	2	1296	$22.0 \pm 0.11^*$	$20.5 \pm 2.6^*$
1 - 800	^{nat}U	2	1296	1.390 ± 0.007	1.24 ± 0.15
1 - 800	^{nat}U	1	1225	0.667 ± 0.004	0.53 ± 0.07
1 - 800	^{nat}U	1	1160	0.787 ± 0.014	0.59 ± 0.07
20 - 800	^{209}Bi	3	1296	0.0041 ± 0.0002	0.0032 ± 0.0004
20 - 800	^{209}Bi	1	1225	0.0014 ± 0.0002	0.00103 ± 0.00013

(*) (see Fig. 7).

(**) The predicted count rates have been re-calculated from the standard proton beam current of 180 μA to the current of 170 μA that represents the average value during the present experiment.

As seen in Table 3, satisfactory agreement is observed between the experimental results and the calculated ones. On the other hand, the experimental count rates systematically exceed the calculated ones by 10-30%.

C. Energy-integrated neutron flux

Experimental count rates extracted from the TOF spectra can be used for calculation of the energy-integrated neutron flux density $\eta_{E_n \min}^{E_n \max}$ with energy above a given value $E_n \min$ in the monitor position by re-writing Eq. (4) in the following form:

$$\eta_{E_n \min}^{E_n \max} = n_{f \exp}(A, p_A) \int_{E_n \min}^{800 \text{ MeV}} \frac{F(E_n, A, p_A)}{s(E_n, A, p_A)} dE_n, \quad (9)$$

where $n_{f \exp}(A, p_A)$ is the experimental count rate of fission events for the given sample (^{nat}U or ^{209}Bi), extracted from the measured TOF spectra by summation of the counts in channels corresponding to neutrons in the energy range 1 - 800 MeV for ^{nat}U samples and 20 - 800 MeV for the ^{209}Bi samples, and $F(E_n, A, p_A)$ is a factor dependent on neutron energy:

$$F(E_n, A, p_A) = \nu(A, p_A) \cdot \varphi(E_n) \cdot k_\varepsilon(E_n, A, p_A) \cdot \sigma_{nf}(E_n, A), \quad (10)$$

where $\nu(A, p_A)$ is a normalization coefficient, which is determined from the condition:

$$\int_{E_n \min(A)}^{800 \text{ MeV}} F(E_n, A, p_A) dE_n = 1, \quad (11)$$

where $E_n \min(A)$ is equal to 1 MeV for ^{nat}U samples and 20 MeV for the ^{209}Bi samples.

Using Eqs. (7, 9 - 11), one can determine the integrated flux $\eta(E_n \min)$, which relates to neutrons with energies above $E_n \min$, using the experimental count rate of fission fragments and the spectral neutron flux density, simulated in [11]:

$$\eta(E_n \min) = \alpha(A, p_A) \cdot \int_{E_n \min}^{800 \text{ MeV}} \varphi(E_n) dE_n, \quad (12)$$

where $\alpha(A, p_A)$ is a constant factor determined from the experimental count rate, $n_{f \exp}(A, p_A)$, for a given monitor sample:

$$\alpha(A, p_A) = \frac{n_{f \exp}(A, p_A)}{p_A \cdot \tilde{\varepsilon}_{sf} \cdot \int_{E_n \min(A)}^{800 \text{ MeV}} \sigma_{nf}(E_n, A) \cdot \varphi(E_n) \cdot k_\varepsilon(E_n, A, p_A) \cdot dE_n}. \quad (13)$$

In Table 4, energy-integrated neutron fluxes above 10 MeV and above 20 MeV are presented at different distances and different monitor sandwiches with ^{nat}U and ^{209}Bi samples. The energy-integrated neutron fluxes are determined using Eq. (12). The quoted uncertainties are statistical only. The experimental results are presented as well in Fig. 9, together with the datum deduced from the calculation in ref. [11], that amounted to $5.48 \cdot 10^4 \text{ cm}^{-2} \text{ s}^{-1}$ (above 10 MeV) and $3.16 \cdot 10^4 \text{ cm}^{-2} \text{ s}^{-1}$ (above 20 MeV) for the reference distance of 1105.5 cm, after recalculation from the standard proton beam current of 180 μA to the current of 170 μA that represents the average value during the present experiment.

Table 4. Experimental energy-integrated neutron flux above 10 MeV.

Energy range	Sample	Distance (cm)	Integrated flux ($\text{cm}^{-2}\text{s}^{-1}$)
10-800 MeV	$^{\text{nat}}\text{U}$	1296	$(4.5\pm 0.4)\cdot 10^4$
10-800 MeV	$^{\text{nat}}\text{U}$	1225	$(5.7\pm 0.4)\cdot 10^4$
10-800 MeV	$^{\text{nat}}\text{U}$	1160	$(6.7\pm 0.5)\cdot 10^4$
20-800 MeV	^{209}Bi	1296	$(3.1\pm 0.2)\cdot 10^4$
20-800 MeV	^{209}Bi	1225	$(3.7\pm 0.5)\cdot 10^4$
20-800 MeV	$^{\text{nat}}\text{U}$	1296	$(2.7\pm 0.2)\cdot 10^4$
20-800 MeV	$^{\text{nat}}\text{U}$	1225	$(3.5\pm 0.3)\cdot 10^4$
20-800 MeV	$^{\text{nat}}\text{U}$	1160	$(4.1\pm 0.3)\cdot 10^4$

As seen from Table 4 and Fig. 9, the experimental results obey approximately the $1/R^2$ law. Provided that the $1/R^2$ law remains valid with the decrease of the distance towards the reference point, the calculation of ref. [11] seems to underestimate the energy-integrated neutron flux by $\sim 20\text{-}30\%$. In addition, the energy-integrated neutron fluxes above 20 MeV, measured with the ^{209}Bi samples, are systematically higher than the ones measured with the $^{\text{nat}}\text{U}$ samples, by $\sim 10\%$.

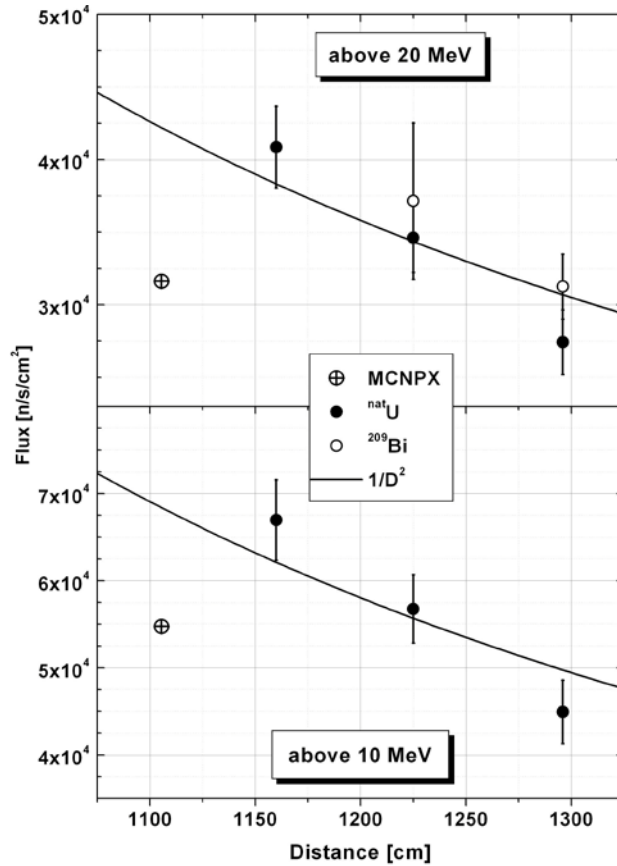


Figure 9. Integrated neutron flux above 10 MeV (lower panel), and above 20 MeV (upper panel) measured with the $^{\text{nat}}\text{U}$ (solid symbols) and ^{209}Bi samples, and calculated with the MCNPX code [11] (an open crossed symbol).

V. ANALYSIS AND DISCUSSION. VERIFICATION OF THE SIMULATED FLUX

A. The count rate ratio $^{nat}\text{U}/^{209}\text{Bi}$

In order to understand the possible reason of the systematic discrepancies between calculated and experimental data, we have studied the sensitivity of calculated count rate ratios for ^{nat}U and ^{209}Bi samples to variations in the simulated spectral neutron flux. In addition to the spectral flux $\varphi_0(E_n)$ from [11], we have tried the following spectral flux functions:

$$\varphi(E_n) = \begin{cases} \varphi_0(E_n), E_n < 1\text{MeV} \\ \varphi_0(E_n) \cdot \left(\frac{E_n}{E_0}\right)^\gamma, E_n > 1\text{MeV} \end{cases}, \quad (14)$$

where $E_0 = 1$ MeV, and γ is a constant, further referred as a *slope factor*. In Fig. 10, the spectral flux functions are shown for $\gamma = -0.2, 0$, and $+0.2$. Count rates for ^{nat}U and ^{209}Bi samples were calculated using Eq. (4). Fig. 11 shows the dependence of the calculated count rate ratios on the variation of the slope factor.

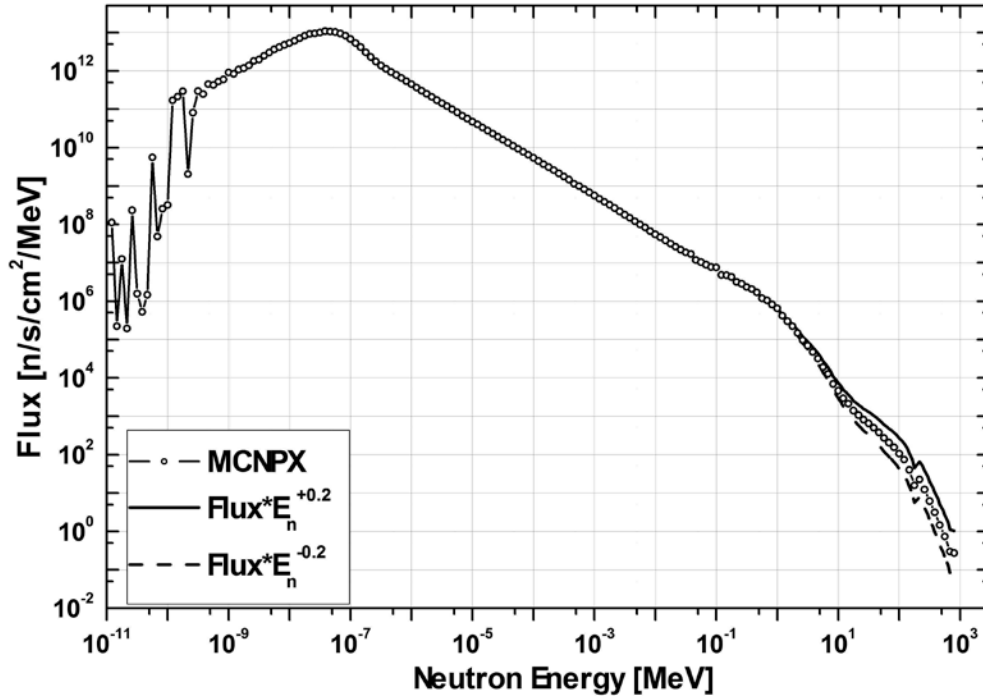


Figure 10. The simulated spectral neutron flux at the VESUVIO instrument at the ISIS neutron source, calculated with the MCNPX code [11] (dots) and its variations above 1 MeV tried in the present work (lines).

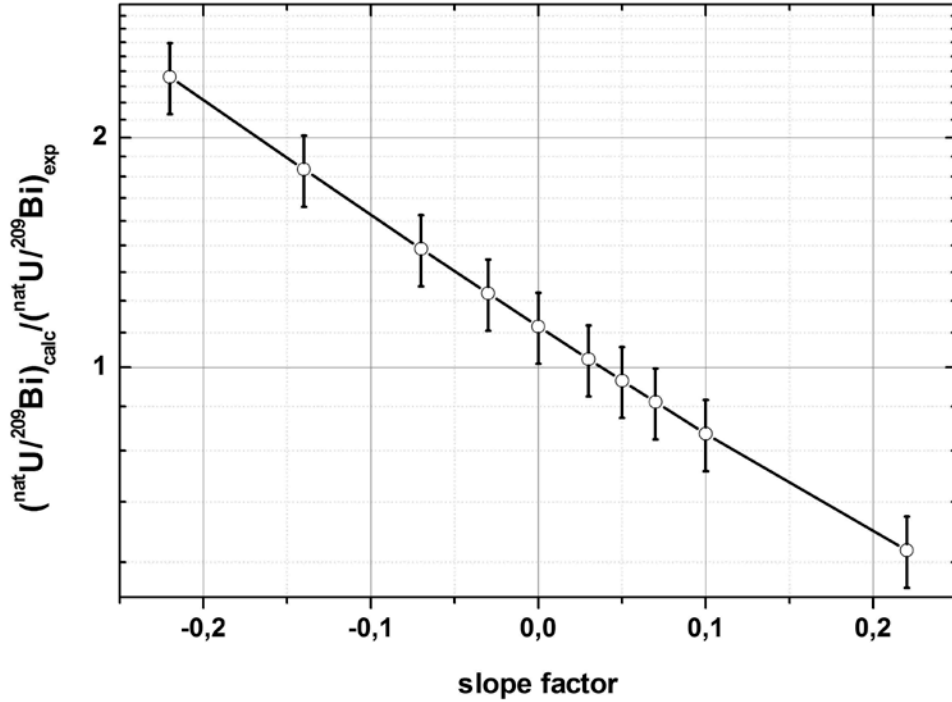


Figure 11. Ratio of calculated and experimental count rate ratios for the ^{209}Bi and ^{238}U samples at the distance of 1296 cm versus the slope factor for the simulated neutron flux.

As seen from Fig. 11, small variations of the slope of the simulated spectral neutron flux result in significant changes of calculated count rate ratios for ^{238}U and Bi monitors. It is seen also that the best agreement of calculated and experimental count rate ratios (ratio = 1) is achieved with the slope factor about 0.03.

Fig. 12 illustrates the sensitivity of the calculated count rates to the presence of neutrons with the highest energies in the spectrum. The count rates for ^{238}U and ^{209}Bi samples were calculated using Eq. (4) with the spectral flux functions extending up to the energy $E_{n\text{ max}}$, which was varied from 200 to 800 MeV. It is seen that, within uncertainties, the calculated count rate ratio is very weakly sensitive to the presence of neutrons with energies above ~500 MeV.

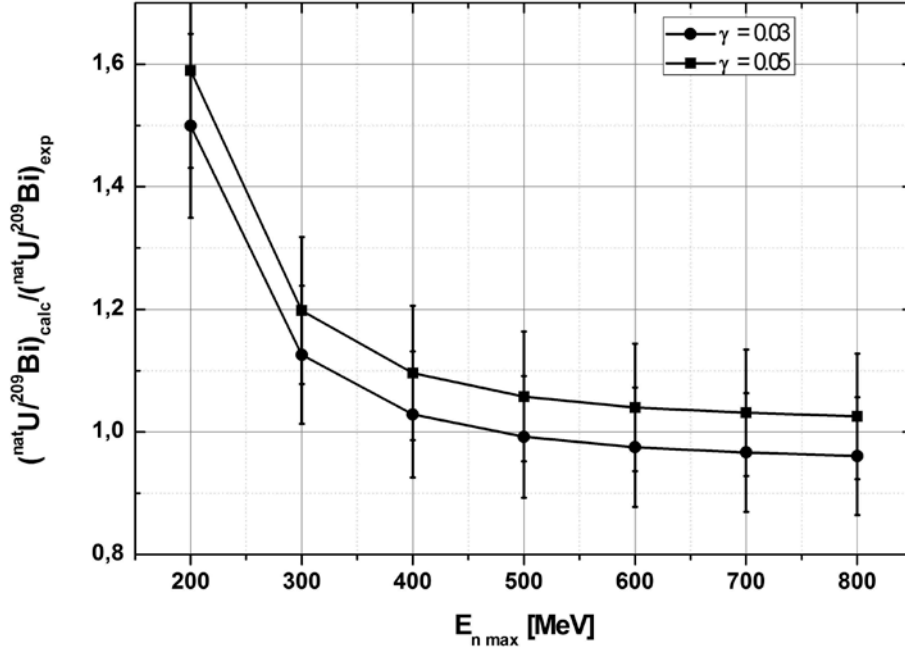


Figure 12. Ratio of calculated and experimental count rate ratios for the ^{nat}U and ^{209}Bi samples at the distance of 1296 cm versus the cut-off energy in the simulated spectral neutron flux.

B. The temporal distributions of fission events

The distribution of fission events on the neutron TOF, shown in Fig. 8, in principle, can be used for the selection of fission events induced by neutrons in different energy ranges.

In Fig. 13, we present TOF spectra of fission events in the ^{209}Bi sample at the distance of 1225 cm (upper panel) and the ^{nat}U sample at the distance of 1296 cm (lower panel), acquired during the same run, together with corresponding spectra simulated using the TFE_MC code. For both the simulations, the same spectral neutron flux [11] has been used. For the $^{nat}\text{U}(n,f)$ TOF spectrum, we present as well the components originating from the first pulse of the primary proton beam in the double-pulsed temporal structure, for the neutron energies above and below 20 MeV, separately (plotted by the dashed and dotted lines, respectively).

As seen from Fig. 13, the “first step” in the *simulated* TOF distribution for $^{nat}\text{U}(n,f)$ is formed exclusively by fission events induced by neutrons with energies from 20 to 800 MeV, which originate from the first pulse of the proton beam in the double-pulsed structure. One can assume that the “first step” in the *experimental* $^{nat}\text{U}(n,f)$ TOF distribution (within the limits of the first 30 channels) is formed by fission events induced by neutrons above 20 MeV, originating from the first proton pulse, too. Thus the “first step” in the *experimental* $^{nat}\text{U}(n,f)$ TOF distribution together with the first peak of the $^{209}\text{Bi}(n,f)$ events can be used for direct determination of the experimental count rate ratio $(^{nat}\text{U}/^{209}\text{Bi})_{\text{exp}}$ for neutrons with the energies above 20 MeV.

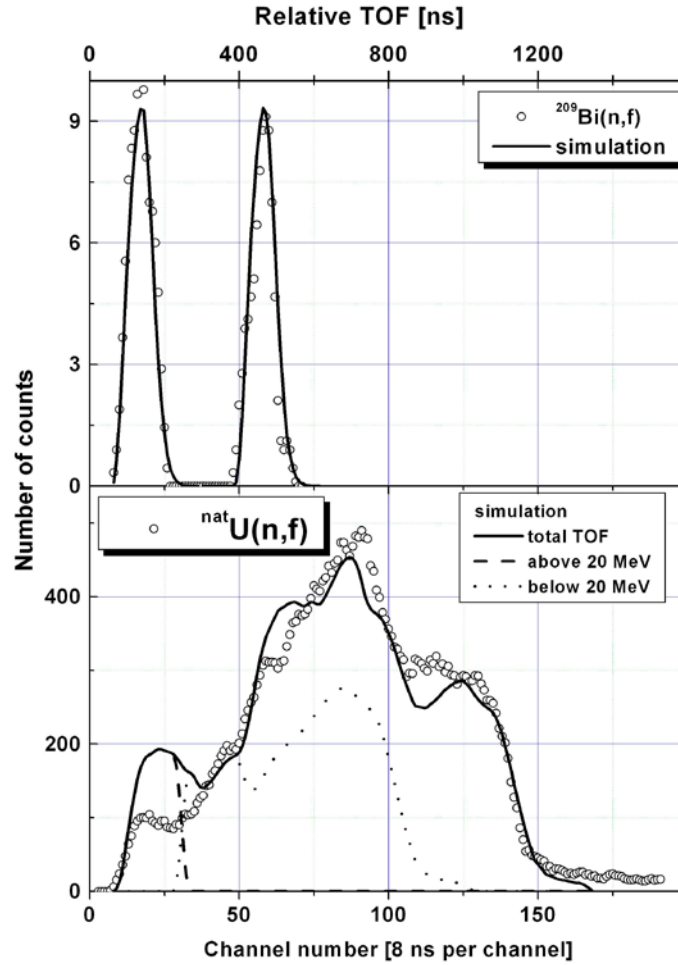


Figure 13. The TOF distributions of fission events in the ^{209}Bi samples at the distance of 1225 cm (upper panel) and $^{\text{nat}}\text{U}$ samples at the distance of 1296 cm (lower panel), and their simulations with the TFE_MC code. Dashed and dot curves at the lower panel represent simulations for the components of spectral neutron flux above and below 20 MeV, respectively, originating from the first proton beam pulse in the double-pulsed temporal structure.

Fig. 14 shows the ratio of the calculated and experimental count rate ratios $(^{\text{nat}}\text{U}/^{209}\text{Bi})_{\text{calc}} / (^{\text{nat}}\text{U}/^{209}\text{Bi})_{\text{exp}}$ above 20 MeV versus the slope factor for the simulated spectral neutron flux. The count rates for $^{\text{nat}}\text{U}$ and ^{209}Bi samples were calculated using Eq. (4) with the lower limit of integration $E_{n \text{ min}} = 20$ MeV. Experimental count rates are derived from the temporal distributions by summation of the fission events within the limits of the “first step” in the $^{\text{nat}}\text{U}$ distribution and within the first peak in the ^{209}Bi distribution.

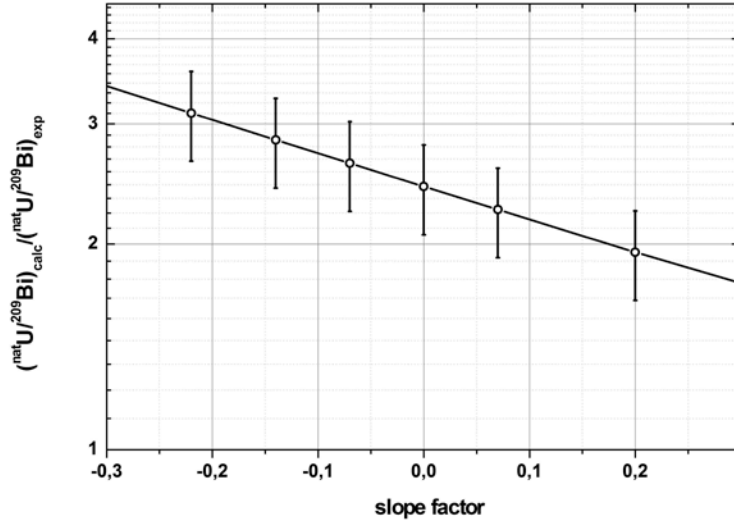


Figure 14. Ratio of calculated and experimental count rate ratios above 20 MeV for the ^{nat}U and ^{209}Bi samples versus slope factor for simulated spectral neutron flux.

As seen from Fig. 14, the ratio does not achieve unity for any reasonable variation of the simulated spectral neutron flux, i.e. it is not possible to reproduce the experimentally obtained count rate ratio $^{nat}\text{U}/^{209}\text{Bi}$. The number of the $^{nat}\text{U}(n,f)$ fission events in the region of the “first step” in the experimental temporal distribution is lower than expected by factor of 2 at least. This disagreement may indicate that the assumption about a point-wise virtual neutron source is not valid. Instead, the data indicate that the position of the “effective neutron source” is dependent on the neutron energy.

In order to match the experiment and the simulation, and thus to explain the observed phenomenon, one needs more detailed simulations of the neutron field at the VESUVIO instrument. Such simulations should include a two-dimensional neutron spectrum, versus both the energy and the “time of arrival” relative to the arrival of the first proton pulse to the production target.

VI. CONCLUSIONS AND OUTLOOK

The presented results of the characterisation run indicate the following:

- i. The TFBC technique is demonstrated and found applicable and highly informative for the characterisation and monitoring of the high-energy part of the ISIS neutron field.
- ii. The simulated spectral neutron flux [11] allows one to reproduce the experimentally obtained count rates of different TFBC-based monitors with deviations not exceeding 30%.
- iii. Systematic disagreement (about 10-30%) between the experimental and simulated count rates can be explained by the following factors, or by their combination:
 - the simulated spectral neutron flux above ~ 1 MeV is underestimated by ~ 20 -30%;
 - the fission cross sections for uranium and bismuth are underestimated in the energy range above ~ 200 MeV, that can lead to the systematic error of not more than 10%;
 - the detection efficiency of the TFBC is underestimated, that can lead to the systematic error of not more than 5%;
 - all target masses are underestimated, that can lead to the systematic error of not more than 3%.

- iv. The calculated count rate ratio $^{nat}\text{U}/^{209}\text{Bi}$ exceeds the experimental one by $\approx 10\%$. In order to reproduce the experimental result, the slope of the simulated neutron spectrum should be gentler at energies above 1 MeV.
- v. The calculated count rate ratio $^{nat}\text{U}/^{209}\text{Bi}$ is very weakly sensitive to the presence of neutrons with energies above ~ 500 MeV.
- vi. The experimental temporal distributions of the ^{nat}U fission events at neutron energies above 1 MeV cannot be reproduced by the simulations. This disagreement may indicate that the assumption about a point-wise virtual neutron source is not valid. Instead, the data indicate that the position of the “effective neutron source” is dependent on the neutron energy.
- vii. More detailed simulations of the neutron field are needed. Such simulations should include a two-dimensional neutron spectrum, versus both the energy and the “time of arrival” relative to the arrival of the first proton pulse to the production target.

VII. ACKNOWLEDGEMENT

We are thankful to ISIS accelerator staff for excellent neutron beam and other support during the beamtime. Thanks to S. Platt, J. Källne, and M. Tardocchi for valuable discussions, and to T. Hartman who kindly helped to organise transportation of samples for the present work. N. P. Filatov made an in-kind contribution to the project by making his TFE_MC and COUCH codes available. A.V. Prokofiev is thankful to TSL management for the positive attitude to the present project, and to the Irradiation Facilities group who got to work harder during his leave from TSL to ISIS. The visit of A.N. Smirnov and A.V. Prokofiev to ISIS was sponsored by CNR, Italy.

VIII. REFERENCES

1. JEDEC Standard JESD89A, “Measurement and reporting of alpha particle and terrestrial cosmic ray-induced soft errors in semiconductor devices”, October 2006, <http://www.jedec.org/download/default.cfm>
2. T. Nakamura, M. Baba, E. Ibe, Y. Yahagi, H. Kameyama, *Terrestrial neutron-induced soft errors in advanced memory devices*, 1st ed., Singapore, World Scientific, 2008, ISBN-13 978-981-277-881-9.
3. <http://lansce.lanl.gov/NS/instruments/ICEhouse/index.html>
4. E.W. Blackmore, Development of a Large Area Neutron Beam for System Testing at TRIUMF, 2009 IEEE Radiation Effects Data Workshop, Quebec, Canada, July 20-24, 2009, pp. 157-160, <http://ieeexplore.ieee.org/stamp/stamp.jsp?arnumber=05336297>, doi:10.1109/REDW.2009.5336297.
5. A. V. Prokofiev, J. Blomgren, M. Majerle, R. Nolte, S. Röttger, S. P. Platt, A. N. Smirnov, “Characterization of the ANITA Neutron Source for Accelerated SEE Testing at The Svedberg Laboratory”, 2009 IEEE Radiation Effects Data Workshop, Quebec, Canada, July 20-24, 2009, pp. 166-173, <http://ieeexplore.ieee.org/stamp/stamp.jsp?arnumber=05336295>, doi:10.1109/REDW.2009.5336295.
6. <http://www.isis.stfc.ac.uk/instruments/Chipir/>
7. <http://ts-2.isis.rl.ac.uk/instruments/phase2/index.htm>
8. V. P. Eismont, A. V. Prokofiev, and A. N. Smirnov, *Radiat. Meas.* 25, 151 (1995).
9. <http://www.fisica.uniroma2.it/~vesuvio/dins/index.html>

10. R. Senesi, C. Andreani, Z. Bowden, D. Colognesi, E. Degiorgi, A. L. Fielding, J. Mayers, M. Nardone, J. Norris, M. Praitano, N. J. Rhodes, W. G. Stirling, J. Tomkinson, and C. Uden, *Physica B* **276–278**, 200 (2000).
11. C. Andreani, et al, *Appl. Phys. Lett.* **92**, 114101 (2008).
12. <http://mcnpx.lanl.gov/>
13. A.N. Smirnov, V.P. Eismont, N.P. Filatov, J. Blomgren, H. Condé, A.V. Prokofiev, P.-U. Renberg, N. Olsson, ‘Measurements of Neutron-Induced Fission Cross-Sections for ^{209}Bi , $^{\text{nat}}\text{Pb}$, ^{208}Pb , ^{197}Au , $^{\text{nat}}\text{W}$, and ^{181}Ta in the Intermediate Energy Region’, *Phys. Rev. C* **70**, 054603 (2004).
14. A.D. Carlson, S. Chiba, F.-J. Hamsch, N. Olsson, and A.N. Smirnov, IAEA Report INDC(NDS)-368, Vienna, 1997; *Proc. Int. Conf. on Nuclear Data for Science and Technology*, Trieste, Italy, May 19-24, 1997, Part II, p. 1223.
15. I.V. Ryzhov et al., *NIM A* **562**, 439-448 (2006).
16. R. Nolte et al., *J. Nucl. Sci. Tech.* 1 (Suppl. 2), 311 (2002).
17. O. Shcherbakov et al., *J. Nucl. Sci. Tech.* 1 (Suppl. 2), 230 (2002).
18. H. Conde, V.P. Eismont, K. Elmgren, A.I. Obukhov, and A.N. Smirnov, ‘A Comparison of Proton- and Neutron-Induced Fission Cross Sections of Heavy Nuclei at Intermediate Energies’, *Proc. of 2nd Int. Conf. on Accelerator-Driven Transmutation Technologies and Applications*, Kalmar, Sweden, June 3-7, 1996, pp. 599-605, published by Uppsala University (1997).
19. A.V. Prokofiev, *Nucl. Instr. and Meth. in Phys. Res.* **A463**, 557 (2001).
20. ENDF/B-VII.0, www.jcprg.org/endl/work/pendl-1932.html
21. N.P. Filatov, personal communication (2000).
22. A. Prokofiev, PhD thesis, Uppsala University (2001).
23. C.M. Zöller, Ph.D. thesis, Darmstadt (1995) (in German).
24. Yu. P. Gangrskiy, B. Dalhsuren, and B. N. Markov, *Nuclear Fission Fragments* (Energoatomizdat, Moscow, 1986) (in Russian).
25. D. Adams, personal communication, September 2009
26. N.P. Filatov, personal communication (2004).
27. A.G. Donichkin, A.N. Smirnov et al. *Nucl. Tracks*. Vol. 3. (1979) p. 205-211
28. <http://www.fastcomtec.com/products/product-lines/ultra-fast-multiscalers/p7888.html>